Theoretical and experimental study of octahedral tilting of Ca$_{1-x}$Gd$_x$MnO$_3$ (x = 0.05, 0.1, 0.15, 0.2) nanometric powders

CrossMark

Milena Rosić [a, *], Dejan Zagorac [a], Dušan Milivojević [b], Novica Paunović [c], Jelena Zagorac [a], Zorana Dohčević-Mitrović [c], Branko Matović [a]

[a] Laboratory for Material Science, Institute of Nuclear Sciences "Vinča", University of Belgrade, P.O. Box 522, 11001 Belgrade, Serbia
[b] Laboratory for Radiation Chemistry and Physics, Institute of Nuclear Sciences "Vinča", University of Belgrade, P.O. Box 522, 11001 Belgrade, Serbia
[c] Center for Solid State Physics and New Materials, Institute of Physics Belgrade, University of Belgrade, Pregrevica 118, 11080 Belgrade, Serbia

ARTICLE INFO

ABSTRACT

In order to estimate theoretical stability of the perovskite structure for synthesized Ca$_{1-x}$Gd$_x$MnO$_3$ (x = 0.05, 0.1, 0.15, 0.2) nanopowders, the Goldschmidt tolerance factor G_t and global instability index *GII* were calculated. Furthermore, we have performed structure prediction of Ca$_{1-x}$Gd$_x$MnO$_3$ perovskites and found several possible perovskite-related phases. The influence of gadolinium amount on Mn–O bond angles and distances, tilting of MnO$_6$ octahedra around all three axes and deformation due to the presence of the Jahn–Teller distortion around Mn^{3+} cation, as well as the influence of the amount of Mn^{3+} cation on Ca$_{1-x}$Gd$_x$MnO$_3$ compound, was examined. Ion Mn valence states were determined by bond valence calculations (BVC). Infrared active phonon modes in Ca$_{1-x}$Gd$_x$MnO$_3$ were studied by infrared reflection spectroscopy and magnetic properties were studied by using EPR (electron para-magnetic resonance) measurements.

1. Introduction

Manganese oxides with perovskite structure, A$_{1-x}$Re$_x$BO$_3$ (A: alkaline earth element, Re: rare earth element, B: Mn, respectively), have become a matter of great scientific interest, because of their physical, electronic and magnetic properties, and many intriguing phenomena, such as colossal magnetoresistance (CMR) involving potential applications in magnetic memory devices and sensors [1–3]. This series of solid solutions with perovskite type of structure is characterized starting from cubic symmetry, usually as a result of small displacements of the oxygen ions and rare earth element from their positions in the ideal cubic unit cell. The compounds of chemical composition Ca$_{1-x}$Gd$_x$MnO$_3$ crystallize in the orthorhombic space group *Pnma*. Smaller Mn ions occupy octahedral 4b (1/2,0,0), while the larger ions, Ca and Gd, take 4c (x, 1/4, z; $x \cong 0$, $z \cong 0$) positions and are surrounded by 12 oxygen atoms residing in the two crystallographic unequivalent positions: O1 in 4c (x, 1/4, z; $x \cong 0$, $z \cong 1/2$) and O2 in 8d (x, y, z; $x \cong 1/4$, $y \cong 0$, $z \cong 1/4$) [4].

In Ca$_{1-x}$Gd$_x$MnO$_3$ compound, valence of Ca, Gd and O ions are +2, +3 and −2, respectively, while Mn ion can be in +3 or +4 valence state. Replacement of Ca^{2+} by Gd^{3+} causes reduction of Mn^{4+} to Mn^{3+} in order to maintain Ca$_{1-x}^{2+}$Gd$_x^{3+}$Mn$_{1-x}^{4+}$Mn$_x^{3+}$O$_3^{2-}$ crystal electroneutrality, which has a significant impact on the physical, and especially on the magnetic properties of these materials. An Mn^{3+} ion has 4 electrons in d orbital (3d^4), while an Mn^{4+} ion has 3 electrons in d orbital (3d^3), and the Mn^{3+}/Mn^{4+} ratio influences magnetic behavior of the system.

Goldschmidt tolerance factor (G_t) has been used as one of the criteria for the degree of distortion of the perovskite lattice. G_t is defined as $Gt = (r_A + r_o)/\sqrt{2}(r_B + r_o)$ [5], where the r_A and r_B correspond to the averaged radii of cations placed in position A (Ca^{2+} and Gd^{3+}) and B (Mn ions), respectively, while r_O represents radius of the oxygen ions. Equation $r_A = (1-x)r_{A'} + xr_d$ gives radius of cation A as the sum of the radius of doped cation $r_{A'}$ and radius of the dopant r_d [6–8]. The relationship between the concentration of dopant x and G_t is $Gt = ((1-x)r_{A'} + xr_d + r_o)/\sqrt{2}(r_B + r_o)$. Any deviation from ideal value Gt = 1, reduces the elementary cubic perovskite cell and leads to formation of a unit cell of lower symmetry. Small difference in the radii of cations placed in positions A leads to a less pronounced rhombohedral distortion, while larger differences give rise to a significant MnO$_6$ octahedron deformation

which leads to orthorhombic structure. This deformation of the MnO_6 octahedron causes anomaly, also known as the Jahn–Teller effect. Namely, removing the degeneracy of the d level of Mn^{3+} ions will lead to the displacement of ions in octahedral MnO_6, where the octahedron will elongate/shorten in certain direction [9]. Perovskite structure can be stable in the oxides where $0.89 < G_t < 1.02$ [9]. Cation will occupy the position in which G_t is closer to 1.

In the octahedral crystal field, fivefold degenerate $3d$ orbitals of manganese are split into two groups, threefold t_{2g} (of lower energy) and twofold e_g (of higher energy) [9]. In accordance with Hund's rules and with fulfillment of the Pauli exclusion principle, $3d$ electrons in the Mn^{4+} ion have the same spins orientation and filled three t_{2g} orbitals, while the Mn^{3+} ion has one electron more, which fills one of the e_g orbitals and has the same spin orientation as electrons in the t_{2g} orbitals. The Jahn–Teller effect causes additional splitting of d energy levels (e_g and t_{2g}) of the Mn^{3+} ions in order to remove their degeneracy, where the splitting of t_{2g} levels is so small that the Jahn–Teller effect in this case is negligible [9–11]. In an octahedral environment manganese t_{2g} orbitals (d_{xy}, d_{yz}, d_{zx}) are the oxygen $2p$ orbitals weakly overlap with, unlike e_g orbitals ($d_{x^2-y^2}$, $d_{3z^2-r^2}$), which are directed towards the neighboring oxygen $2p$ orbitals and a strong overlapping of these orbitals leads to a high probability of transfer of electrons between manganese and oxygen orbitals [9–11]. This transfer largely determines the magnetic properties of manganites.

Magnetic properties of this mixed valence system are determined by a double exchange between Mn^{3+} and Mn^{4+} ions through the Mn–O–Mn path. The double exchange is ferromagnetic for Mn–O–Mn angle above ~160° [12–17]. When the system is doped with different Gd^{3+} concentrations, it develops ferromagnetic interaction concurrently with antiferromagnetic one and competition of the interactions causes magnetic moments frustration.

In this study we have combined two research methods: structure prediction of $Ca_{1-x}Gd_xMnO_3$ ($x = 0.05, 0.1, 0.15, 0.2$) perovskites by using computational SPuDS software, and characterization of the studied perovskites. We have shown various possible modifications of $Ca_{1-x}Gd_xMnO_3$ ($x = 0.05, 0.1, 0.15, 0.2$) perovskites, unknown so far. Also, we have investigated the influence of Gd doping on octahedral tilting, relation between the crystal structures which have been predicted, and structural and magnetic behavior we have experimentally observed.

2. Material and methods

2.1. Experimental section

2.1.1. Theoretical methods

Our general approach to the crystal structure prediction and determination of structure candidates has been given in detail elsewhere [18–20]. This is usually followed by calculation of material's properties [21,22]. Here, we use restricted structure prediction within the perovskite-related structures. An outline of the main steps of the method and information specific to this study are provided first.

The Structure Prediction Diagnostic Software (SPuDS) [23] has been used to produce new structure candidates of $Ca_{1-x}Gd_xMnO_3$ perovskites. The SPuDS program was developed to predict the crystal structures of perovskites, including those distorted by tilting of symmetric octahedra or caused by the Jahn–Teller distortions [20,24]. Stability of the perovskite structures is determined by comparing the calculated bond-valence sums and ideal formal valences.

The SPuDS program requires minimum amount of input data: the composition and oxidation state of each ion. Afterwards, structure optimization has been performed by restricting the

octahedra to remain rigid during calculation, with six equivalent B-X distances and all X-B-X angles equal to 90°. In this way, a full crystal structure can be generated from the size of the octahedron and magnitude of the octahedral tilting distortion. Furthermore, SPuDS calculates the fractional position of each atom at each tilt angle step over a wide range of octahedral tilt angles [23].

The size of the octahedron and magnitude of the octahedral tilting distortion are calculated by using the bond valence model, s_{ij},

$$S_{ij} = e^{[(Rij-dij)/B]} \tag{1}$$

where d_{ij} is cation–anion distance, B parameter is empirically determined as a universal constant with a value of 0.37, and R_{ij} is empirically determined for each cation–anion pair, based on bond distances measurements. The overall structure stability is determined by comparing the calculated bond valence sums with the ideal formal valences (equal to oxidation state). This quantity is known as the global instability index (GII). It is calculated according to relation [23]:

$$GII = \left\{ \left[\sum_{i=1}^{N} \left(d_i^2 \right) \right] \bigg/ N \right\}^{1/2} \tag{2}$$

Variables involved in the GII equation are discrepancy factor d_i, which is a measure of the lattice strains present in the compound, derived as a difference between formal and calculated bond valance, and N is the number of atoms in the asymmetric unit. For the perovskite ABO_3, $N = 5$. Higher values of d_i and N indicate stressed connections which can lead to instability in the crystal structure.

Theoretical determination and identification of the predicted structures was performed by using the KPLOT program [25]. Symmetry of the predicted structures was analyzed by the algorithms SFND („Symmetry FiNDer" [26]) and RGS („Raum Gruppen Sucher" or space group seeker [27]). Duplicate structures are removed by using the CMPZ-algorithm [28] and the CCL algorithm has been used in the investigation of nanosized structures [29]. The investigated structures were visualized by using KPLOT [25] and VESTA [30] software.

2.2. Experimental methods

2.2.1. Materials synthesis

The method of preparation, conditions of synthesis, obtained values for the calcination temperature, and crystal-structural characteristics of the $Ca_{1-x}Gd_xMnO_3$ ($x = 0.05, 0.1, 0.15, 0.2$) samples are described in [31] and [32]. The unit cell parameters of this series of samples were identical to the values obtained in [32].

2.2.2. Materials characterization

XRD patterns of the samples were recorded at room temperature by using X-ray diffractometer Siemens D500 with nickel filtered CuKα radiation, and the step-scan mode (2θ range: 10° - 80° in a continuous scan mode with a step width of 0.02° and exposure of 10 s/step).

The infrared reflectivity measurements were performed at room temperature with a BOMEM DA-8 Fourier-transform IR spectrometer. A Hyper beamsplitter and a deuterated triglycine sulfate (DTGS) pyroelectric detector were used to cover the wavenumber region from 80 to 650 cm^{-1}. Infrared reflectivity spectra were collected with 2 cm^{-1} resolution and with 500 interferometer scans added for each spectrum.

EPR experiments were performed on an X-band Magnettech MS300 spectrometer operating at a nominal frequency of 9.5 GHz. The microwave power was 3.16 mW (microwave attenuation

15 dB), with a modulation amplitude of 0.2 mT. The Magnettech g-factor ZnS:Mn standard was used as the reference sample.

3. Results and discussion

3.1. Crystallographic analysis of XRD the results and investigation of octahedral tilting

Octahedral tilting is most common in the perovskites with space group *Pnma*. Perovskite structure which crystallizes in this space group is of great interest for geologists and materials science [33]. *Pnma* space group belongs to the $a^-b^+a^-$ octahedron tilting system. Octahedra are rotated by the same value of the angle around axes a and c, whereas the angle of rotation around axis b varies. Rotations of two adjacent octahedra along axis b are always in the same direction, and along axes a and c in the opposite direction. There are two types of deformations in the space group *Pnma*, denoted as *Pnma-1* and *Pnma-2*. Both of them have the same symmetry, but *Pnma-1* is much less deformed and only slightly deviates from the cubic structure. *Pnma-2* contains more distorted octahedra due to the Jahn−Teller effect caused by Mn^{3+} ions, which leads to elongation of the MnO_6 octahedron [8]. Our obtained results suggest that investigated samples have the *Pnma-1* structure.

In order to analyze the impact of Gd upon magnitude of the octahedral tilting, we have analyzed values of the Mn−O distances and angles. The characteristic distances and angles between Mn, O1 and O2 atoms are shown in Table 1. Average values of interatomic distances Mn−O vary with the amount of Gd in the structure. The highest value has the $Ca_{0.8}Gd_{0.2}MnO_3$ sample, where the content of Gd is the highest. In our previous work we have published data on the unit cell parameters and volumes depending on Gd concentration [32], and in the following Table 1 we have further investigated interatomic distances and bond angles of $CaMnO_3$ doped with different concentrations of Gd.

Octahedra nets for each of the investigated samples are given in Fig. 1. As one can see from Fig. 1, structural changes related to the change of angle values lead only to a slight octahedral tilting. In an ideal cubic structure the Mn−O1−Mn and Mn−O2−Mn angles are 180°. Because of the octahedral tilting around all three axes in the space group *Pnma* the angle values will be different. Mn−O1−Mn angle represents tilting around axis b and for the obtained samples, the closest to 180° is the value for $Ca_{0.8}Gd_{0.2}MnO_3$ sample (Table 1). On the other side, Mn−O2−Mn angle represents octahedral tilting around axes a and c and the magnitude of octahedral tilting (angle)

is in accordance with the $a^-b^+a^-$ tilt system. In the structure, with increasing Gd amount, the deviation from 180° and octahedral tilting magnitude are higher (Table 1). In the cube centers, oxygen ions tend to move toward that center reducing d_{A-O}, because A ions are too small to fill that space. At the same time d_{Mn-O} also changes, and the Mn−O−Mn angle becomes smaller than 180° as a result of the reduced A-site radius [11].

The properties of manganites strongly depend on geometrical quantity G_t [11], which is related to the displacements and deformations in the structure. Difference in the lengths of $A−O$ and $B−O$ bonds has been used as a measure of G_t change: $G_t = (A-O)/\sqrt{2}(B-O)$. In the case when bonds $B−O$ are lengthened and $A−O$ shortened, $G_t < 1$ [8]. Since G_t for all investigated samples is less than 1 and close to 0.93 (calculation based on the bond lengths obtained by Rietveld analysis given in Table 1), we can conclude that in our system occurred elongations of Ca−O and shortenings of Mn−O bonds. The structure alleviates these strains by BO_6 octahedron rotation, which leads to a reduction of symmetry.

We have also analyzed the effects of concentration of gadolinium on octahedral deformations. For $Ca_{1-x}Gd_xMnO_3$ ($x = 0.05, 0.1, 0.15, 0.2$) samples, interatomic Mn−O distances inside octahedra are shown in Fig. 2. In ac plane lies the shortest octahedral Mn−O2 bond, which is represented by the first and third bar in Fig. 2. In b-axis direction lies the intermediate octahedral Mn−O1 bond, represented by the third bar. The octahedral deformation occurs as a result of the Mn−O distances deviation. The deviation of the Mn−O (dn) distances with respect to the average <Mn−O> ($<d>$) value defines the distortion of the octahedra [34]: $\Delta = (1/6)\sum_{n=1,6}[(d_n - \langle d \rangle)/\langle d \rangle^2]$.

Here, we observe that with an increase of Gd^{3+} content in the structure, difference between the longest and shortest distances increases non-periodically (see Fig. 2). The octahedral deformations indicate the presence of oxygen vacancies caused by reduction of Mn^{4+} to Mn^{3+} due to Gd doping. We note that 10% of the Gd increase in the system has the highest Δ value, which has been used as indication of the Jahn Teller distortion in the structure [34].

The Jahn−Teller effect can be observed by comparing the results obtained for individual Mn−O bond lengths, leading to the conclusion that there has been a change in the valence state of Mn^{4+} i.e. reduction to Mn^{3+}. Rhombohedral and octahedral distortion increases with Gd doping. Increase of Mn^{3+} concentration with Gd doping increases the average Mn−O bond length in the unit cell (for $Mn^{3+}−O$ it is 2.04 Å, and for $Mn^{4+}−O$, 1.88 Å [35]).

Table 1
Interatomic distances and bond angles for investigated samples of $Ca_{1-x}Gd_xMnO_3$ ($x = 0.05, 0.1, 0.15, 0.2$).

Sample	$Ca_{0.95}Gd_{0.05}MnO_3$		$Ca_{0.9}Gd_{0.1}MnO_3$	$Ca_{0.85}Gd_{0.15}MnO_3$	$Ca_{0.8}Gd_{0.2}MnO_3$
$\langle Ca-O \rangle$	2.5759		2.5270	2.5798	2.5304
Ca−O	2×	2.635 (5)	2.6736 (3)	2.6612 (1)	2.7537 (3)
	2×	2.340 (4)	2.3163 (3)	2.36131 (1)	2.3225 (1)
		2.970 (8)	2.9163 (6)	2.9626 (4)	2.9303 (4)
		2.887 (9)	2.3073 (6)	2.9061 (3)	2.3237 (4)
		2.380 (7)	2.4647 (5)	2.3791 (3)	2.4453 (4)
	2×	2.557 (5)	2.5403 (3)	2.5252 (2)	2.4609 (1)
		2.458 (8)		2.4544 (3)	
$\langle Mn-O \rangle$	1.91023		1.91321	1.90885	1.92102
Mn−O	2×	1.8978 (10)	1.84859 (5)	1.90684 (3)	1.88364 (4)
	2×	1.9335 (9)	1.97726 (6)	1.91820 (3)	1.96677 (4)
	2×	1.8994 (7)	1.91378 (5)	1.90151 (2)	1.91264 (3)
O2−Mn−O2	91.32 (9)		91.144 (5)	91.1051 (16)	90.6 (10)
O1−Mn−O1	180.00 (9)		180.000 (6)	179.972 (3)	180.000 (4)
Mn−O1−Mn	159.21 (9)		155.092 (6)	159.294 (3)	162.592 (4)
Mn−O2−Mn	157.16 (11)		156.603 (6)	157.147 (2)	155.6 (5)
Mn(BCV)	3.927		3.931	3.938	3.826
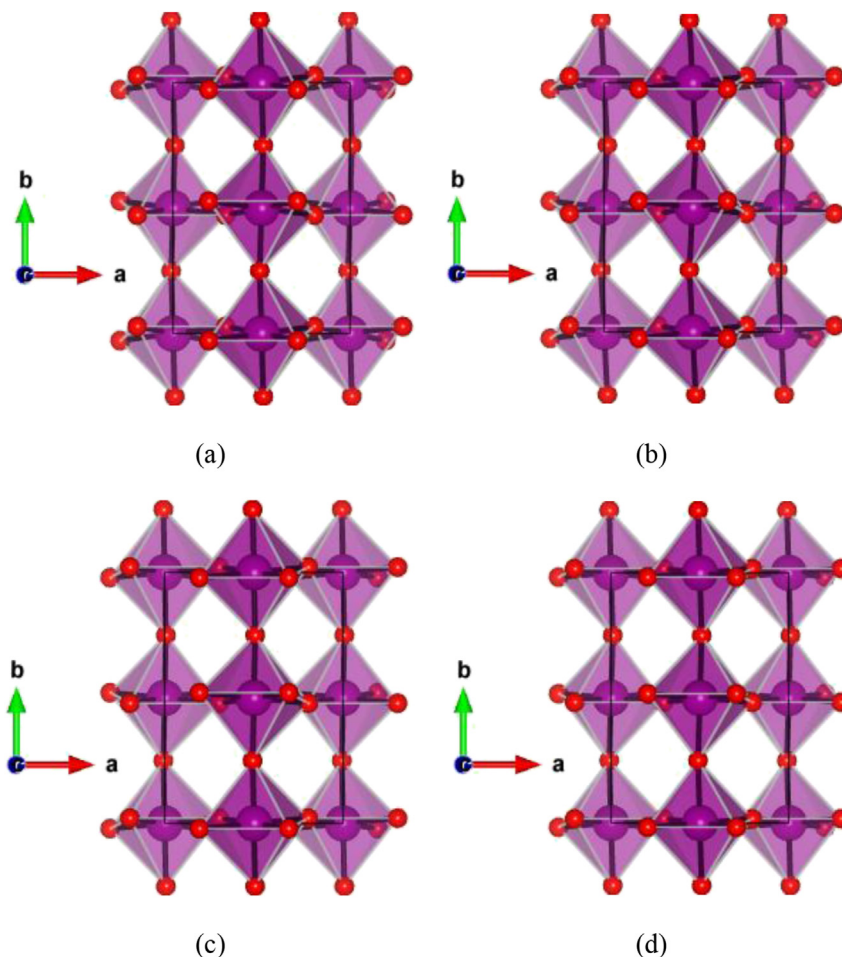
Fig. 1. Octahedral net of perovskite phase in a) $Ca_{0.95}Gd_{0.05}MnO_3$; b) $Ca_{0.9}Gd_{0.1}MnO_3$; c) $Ca_{0.85}Gd_{0.15}MnO_3$; d) $Ca_{0.8}Gd_{0.2}MnO_3$ sample.
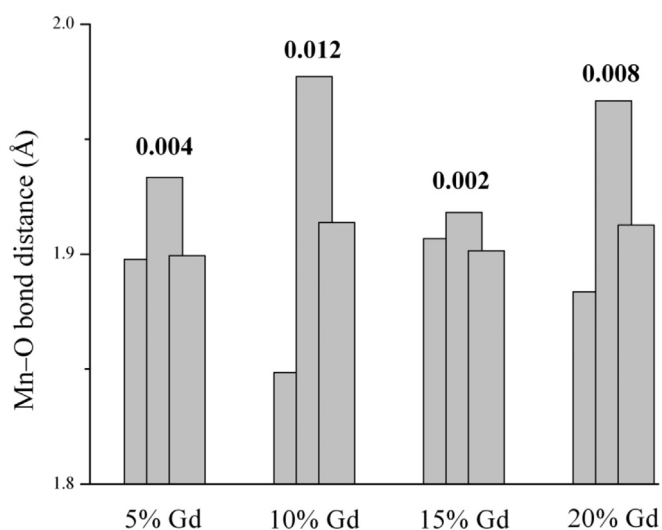

Fig. 2. Interatomic Mn–O distances of the investigated samples of $Ca_{1-x}Gd_xMnO_3$ ($x = 0.05, 0.1, 0.15, 0.2$) perovskites. The values of Δ are given above bars.

In addition, for each sample the Mn–O distance systematically increases compared to the average Mn–O distance, clearly indicating that the octahedral expansion is essentially a result of the *a-c* basal plane increase as a consequence of Gd^{3+} entering Ca^{2+}

position. Of essential importance is the ratio of ionic radii and co-valent nature of the Mn–O bond. There is clearly visible difference between the apical (Mn–O1) and equatorial (Mn–O2) distances in MnO_6 octahedron for all four samples. Difference in the Mn–O bond lengths indicates occurrence of oxygen vacancies. Further-more, by comparing the apical and equatorial bonds with the re-sults for undoped $CaMnO_3$ [36,37] we can conclude that there is an octahedral tilting in the doped samples. With an increase of the content of Gd in the structure, the deviations are increased pointing at a significant tilting of octahedrons. Based on the previously mentioned, in the $Ca_{1-x}Gd_xMnO_3$ ($x = 0.05, 0.1, 0.15, 0.2$) samples, MnO_6 octahedrons cannot be described by six nearly equal Mn–O distances. The octahedrons of doped samples are distorted and the expansions are not the same in all three directions. As expected, changes in the bond lengths with increased content of Gd are very similar to the changes in the unit cell parameters [32]. These results clearly show that there is a close connection between the unit cell parameters and presence of the Jahn–Teller distortion due to the presence $Mn^{3+}O_6$ octahedron oriented in *ac* plane.

3.2. Structure prediction of $Ca_{1-x}Gd_xMnO_3$ perovskites

After performing the structure prediction calculations for $Ca_{1-x}Gd_xMnO_3$ by using SPuDS software, we obtained the equilib-rium *Pnma* structure and ten additional perovskite-related modi-fications, presented in Tables A.1–A.4 (see the Supporting Information). Each of the calculated $Ca_{1-x}Gd_xMnO_3$ modifications

(marked by 1−10) was sorted by its space group and *GII* values (see Tables 2−5). Here we would like to point out that instability of the CaMnO$_3$ system grows with increase of Gd doping (See Fig. 3). Fig. 3 shows the stability of the most favorable perovskite-related structures with Gd increasing the content of Gd in the CaMnO$_3$ system.

The *Pnma* phase is the most stable form of Ca$_{1-x}$Gd$_x$MnO$_3$, which is in agreement with our experimental findings [32]. Furthermore, we have observed that in the case of a low Gd doping (less than 15%), the $R\bar{3}c$ modification (Ca$_{0.95}$Gd$_{0.05}$MnO$_3$-(2)) is the most stable form next to the equilibrium *Pnma* structure, according to the *GII* values. With an increase of Gd in the system (>20%, see Table 5), we have observed possible orthorhombic (Ca$_{0.8}$Gd$_{0.2}$MnO$_3$-(5), *Pnma*) − tetragonal (Ca$_{0.8}$Gd$_{0.2}$MnO$_3$-(5), *P4$_2$/nmc*), rather than orthorhombic (Ca$_{0.8}$Gd$_{0.2}$MnO$_3$-(5), *Pnma*) − trigonal (Ca$_{0.8}$Gd$_{0.2}$MnO$_3$-(5), $R\bar{3}c$) phase transition. After analyzing the Ca$_{1-x}$Gd$_x$MnO$_3$ predicted structures in Figs. 1 and 4, we observed that Gd was homogeneously distributed over the crystal structure. Also, we noted that in the sample doped with 5% of Gd, the most unstable form was orthorhombic Ca$_{0.95}$Gd$_{0.05}$MnO$_3$-(10) (*I4/mmm*) modification, whereas with a larger amount of doping, the cubic perovskite (Ca$_{0.8}$Gd$_{0.2}$MnO$_3$-(8)) became the most unstable form of Ca$_{1-x}$Gd$_x$MnO$_3$ (see Tables 2−5 and Fig. 4). Similar trends were observed in the previous research with pure CaMnO$_3$ compound by using *ab inito* methods [20]. This change of symmetry is due to distortions away from the ideal perovskite structure that occur at different tilt systems.

Bond valence calculations (BVC) often resulted in a Mn valence state higher than the nominal value and the reason being strong Mn−O bond [38]. For the Ca$_{1-x}$Gd$_x$MnO$_3$ system we have also noticed higher values for BVC than expected, in view of the presence of Mn^{3+} in these perovskites, which could reduce valence state of Mn. In the next step we have compared our calculated and experimentally observed *Pnma* structure in the Ca$_{1-x}$Gd$_x$MnO$_3$ system (see Table 6). Our SPuDS calculations show slight decrease of unit cell volume, whereas in the experiment we observed quite the opposite result, a slight increase of cell volume. This discrepancy originates from the appearance of Mn^{3+} and, as it was pointed out before, these results clearly show that there is a close connection between the unit cell parameters and the presence of the Jahn−Teller distortion due to the presence Mn^{3+}O$_6$ octahedron.

Furthermore, following these results, we have managed to calculate the amount of Mn^{4+} and Mn^{3+} in the doped perovskite compound which, to the best of our knowledge, has never been calculated before, at least not in this way. Due to the fact that cell volume is connected to the presence of Mn^{3+} in the system (see above), at first, we have calculated change of the equilibrium volume as a result of Gd doping. The results showed that total cell volume of the investigated perovskite system has been increased by ~0.01% in the sample doped with 5% of Gd (see Table 6).

Table 2
Calculated values of the global instability index (*GII*) for ten Ca$_{0.95}$Gd$_{0.05}$MnO$_3$ modifications using SPuDS software.

| Name	Space group	Tilt system	*GII* (a.u.)
Ca$_{0.95}$Gd$_{0.05}$MnO$_3$-(1)	*Pnma*	$a^-b^+a^-$	0.03969
Ca$_{0.95}$Gd$_{0.05}$MnO$_3$-(2)	$R\bar{3}c$	$a^-a^-a^-$	0.08593
Ca$_{0.95}$Gd$_{0.05}$MnO$_3$-(3)	*P4/mbm*	$a^0a^0c^-$	0.09058
Ca$_{0.95}$Gd$_{0.05}$MnO$_3$-(4)	*I4/mcm*	$a^0a^0c^-$	0.09058
Ca$_{0.95}$Gd$_{0.05}$MnO$_3$-(5)	*P4$_2$/nmc*	$a^+a^+c^-$	0.10742
Ca$_{0.95}$Gd$_{0.05}$MnO$_3$-(6)	*Im$\bar{3}$*	$a^+a^+a^+$	0.12980
Ca$_{0.95}$Gd$_{0.05}$MnO$_3$-(7)	*Cmcm*	$a^+b^0c^-$	0.14282
Ca$_{0.95}$Gd$_{0.05}$MnO$_3$-(8)	*Pm$\bar{3}$m*	$a^0a^0a^0$	0.15494
Ca$_{0.95}$Gd$_{0.05}$MnO$_3$-(9)	*Imma*	$a^0b^-b^-$	0.16295
Ca$_{0.95}$Gd$_{0.05}$MnO$_3$-(10)	*I4/mmm*	$a^0b^+b^+$	0.16468

Table 3
Calculated values of the global instability index (*GII*) for ten Ca$_{0.9}$Gd$_{0.1}$MnO$_3$ modifications using SPuDS.

Name	Space group	Tilt system	*GII* (a.u.)
Ca$_{0.9}$Gd$_{0.1}$MnO$_3$-(1)	*Pnma*	$a^-b^+a^-$	0.05667
Ca$_{0.9}$Gd$_{0.1}$MnO$_3$-(2)	$R\bar{3}c$	$a^-a^-a^-$	0.09777
Ca$_{0.9}$Gd$_{0.1}$MnO$_3$-(3)	*P4/mbm*	$a^0a^0c^-$	0.10236
Ca$_{0.9}$Gd$_{0.1}$MnO$_3$-(4)	*I4/mcm*	$a^0a^0c^-$	0.10236
Ca$_{0.9}$Gd$_{0.1}$MnO$_3$-(5)	*P4$_2$/nmc*	$a^+a^+c^-$	0.10742
Ca$_{0.9}$Gd$_{0.1}$MnO$_3$-(6)	*Im$\bar{3}$*	$a^+a^+a^+$	0.12980
Ca$_{0.9}$Gd$_{0.1}$MnO$_3$-(7)	*Cmcm*	$a^+b^0c^-$	0.14282
Ca$_{0.9}$Gd$_{0.1}$MnO$_3$-(9)	*Imma*	$a^0b^-b^-$	0.15765
Ca$_{0.9}$Gd$_{0.1}$MnO$_3$-(10)	*I4/mmm*	$a^0b^+b^+$	0.16468
Ca$_{0.9}$Gd$_{0.1}$MnO$_3$-(8)	*Pm$\bar{3}$m*	$a^0a^0a^0$	0.17129

Table 4
Calculated values of the global instability index (*GII*) for ten Ca$_{0.85}$Gd$_{0.15}$MnO$_3$ modifications using SPuDS.

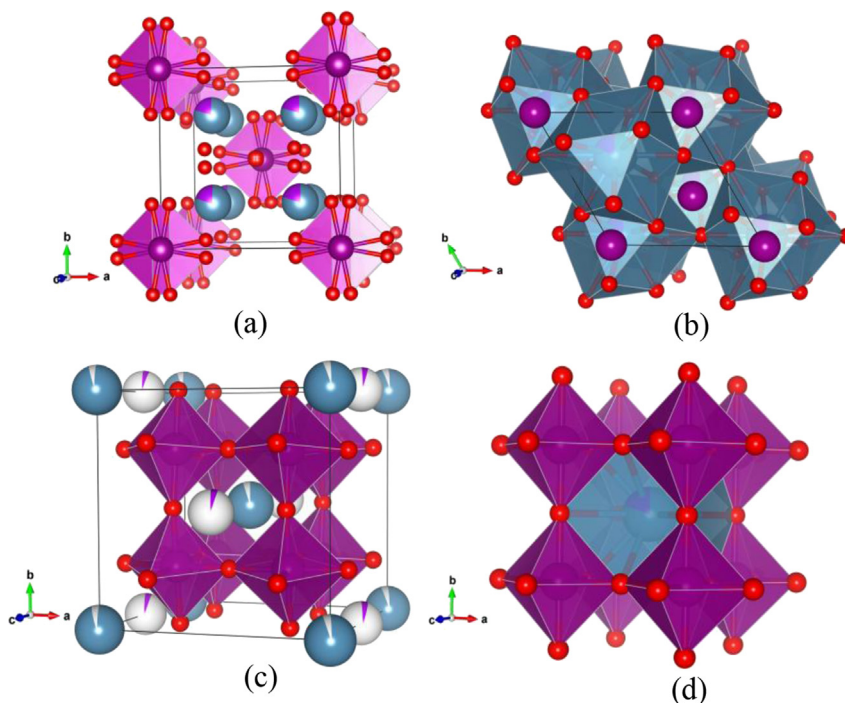| Name	Space group	Tilt system	*GII* (a.u.)
Ca$_{0.85}$Gd$_{0.15}$MnO$_3$-(1)	*Pnma*	$a^-b^+a^-$	0.07013
Ca$_{0.85}$Gd$_{0.15}$MnO$_3$-(2)	$R\bar{3}c$	$a^-a^-a^-$	0.10740
Ca$_{0.85}$Gd$_{0.15}$MnO$_3$-(5)	*P4$_2$/nmc*	$a^+a^+c^-$	0.10742
Ca$_{0.85}$Gd$_{0.15}$MnO$_3$-(3)	*P4/mbm*	$a^0a^0c^-$	0.11204
Ca$_{0.85}$Gd$_{0.15}$MnO$_3$-(4)	*I4/mcm*	$a^0a^0c^-$	0.11204
Ca$_{0.85}$Gd$_{0.15}$MnO$_3$-(6)	*Im$\bar{3}$*	$a^+a^+a^+$	0.12980
Ca$_{0.85}$Gd$_{0.15}$MnO$_3$-(7)	*Cmcm*	$a^+b^0c^-$	0.14282
Ca$_{0.85}$Gd$_{0.15}$MnO$_3$-(9)	*Imma*	$a^0b^-b^-$	0.15304
Ca$_{0.85}$Gd$_{0.15}$MnO$_3$-(10)	*I4/mmm*	$a^0b^+b^+$	0.16468
Ca$_{0.85}$Gd$_{0.15}$MnO$_3$-(8)	*Pm$\bar{3}$m*	$a^0a^0a^0$	0.18620
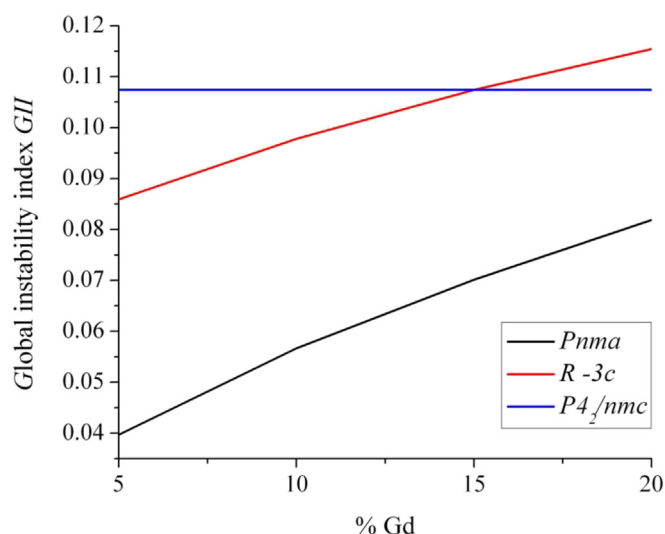
Fig. 3. Phase transition from *Pnma*, $R\bar{3}c$ to *P4$_2$/nmc* with Gd ion increase in CaMnO$_3$ compound.

Next, we have calculated different compositions of Mn^{4+} and Mn^{3+} for the same amount of Gd doping (see Table A.5 in the Supporting Information). We have discovered that the cell volume started to increase, as we obtained by the experiment (see Table 6). In addition, we noted that the best fit for the volume cell increase for 5% of Gd, was obtained for 5% increase of Mn^{3+} in the system, which is ~0.01%, the predicted volume increase and is in very good agreement with our experimental observations. Therefore, we can conclude that with 5% Gd increase in the Ca$_{1-x}$Gd$_x$MnO$_3$ system, we could expect 5% Mn^{3+} increase in the system. Finally, we show the

Table 5
Calculated values of the global instability index (*GII*) for ten $Ca_{0.8}Gd_{0.2}MnO_3$ modifications using SPuDS.

Name	Space group	Tilt system	GII (a.u.)
$Ca_{0.8}Gd_{0.2}MnO_3$-(1)	*Pnma*	$a^-b^+a^-$	0.08188
$Ca_{0.8}Gd_{0.2}MnO_3$-(5)	*P4₂/nmc*	$a^+a^+c^-$	0.10742
$Ca_{0.8}Gd_{0.2}MnO_3$-(2)	$R\bar{3}c$	$a^-a^-a^-$	0.11544
$Ca_{0.8}Gd_{0.2}MnO_3$-(3)	*P4/mbm*	$a^0a^0c^-$	0.12018
$Ca_{0.8}Gd_{0.2}MnO_3$-(4)	*I4/mcm*	$a^0a^0c^-$	0.12018
$Ca_{0.8}Gd_{0.2}MnO_3$-(6)	$Im\bar{3}$	$a^+a^+a^+$	0.12980
$Ca_{0.8}Gd_{0.2}MnO_3$-(7)	*Cmcm*	$a^+b^0c^-$	0.14282
$Ca_{0.8}Gd_{0.2}MnO_3$-(9)	*Imma*	$a^0b^-b^-$	0.14936
$Ca_{0.8}Gd_{0.2}MnO_3$-(10)	*I4/mmm*	$a^0b^+b^+$	0.16468
$Ca_{0.8}Gd_{0.2}MnO_3$-(8)	$Pm\bar{3}m$	$a^0a^0a^0$	0.20001

phonon features at 286/336 cm^{-1}, 416 cm^{-1} and 556 cm^{-1}, together with a pronounced Drude-like contribution from free charge carriers, which dominates the reflectivity spectra in the range below 200 cm^{-1}, can be seen. The perovskite manganites usually have three strong phonon bands, known as external, bending and stretching modes, located at about 150−180, 350, and 550-600 cm^{-1} respectively [39−42]. For the ideal cubic perovskite structure $AMnO_3$ (space group $Pm\bar{3}m$), the factor group analysis predicts three 3-fold degenerated IR active modes of F_{1u} symmetry. The lowest energy F_{1u} mode (the external mode) originates from vibrations of A cation against MnO_6 octahedra, and it is usually found in 150−180 cm^{-1} range. The medium energy F_{1u} mode (the bending mode) originates from bending of Mn−O bonds in the

Fig. 4. Visualization of several calculated perovskite-related structures a) $Ca_{0.8}Gd_{0.2}MnO_3$-(5), $P4_2/nmc$; b) $Ca_{0.8}Gd_{0.2}MnO_3$-(2), $R\bar{3}c$; c) $Ca_{0.95}Gd_{0.05}MnO_3$-(10), (*I4/mmm*); d) cubic perovskite $Ca_{0.8}Gd_{0.2}MnO_3$-(8), ($Pm\bar{3}m$).

Table 6
Unit cell parameters and volumes of the experimentally observed and calculated (SPuDS) equilibrium *Pnma* structure in $Ca_{1-x}Gd_xMnO_3$ system.

Sample		$Ca_{0.95}Gd_{0.05}MnO_3$		$Ca_{0.9}Gd_{0.1}MnO_3$		$Ca_{0.85}Gd_{0.15}MnO_3$		$Ca_{0.8}Gd_{0.2}MnO_3$	
Method		Experiment	SPuDS	Experiment	SPuDS	Experiment	SPuDS	Experiment	SPuDS
Unit cell parameters (Å)	*a*	5.2834 (5)	5.3576	5.304 (1)	5.3569	5.3152 (9)	5.3562	5.3186 (5)	5.3555
	b	7.4665 (6)	7.5407	7.475 (1)	7.5385	7.4795 (8)	7.5366	7.4792 (7)	7.5347
	c	5.2994 (4)	5.3073	5.293 (1)	5.3051	5.303 (1)	5.3030	5.3003 (7)	5.3011
Volume (Å³)	*V*	209.03 (3)	214.415	209.84 (7)	214.237	210.81 (6)	214.069	210.84 (7)	213.912

calculated structures for $Ca_{1-x}Gd_xMn_{1-x}^{4+}Mn_x^{3+}O_3$ system obtained by using SPuDS software. In Tables A.1−A.4 (see the Supporting Information) we the present unit cell parameters for ten additional perovskite-related modifications.

3.3. Infrared (IR) spectroscopy

IR reflectivity spectra of the $Ca_{1-x}Gd_xMnO_3$ samples in 80−650 cm^{-1} spectral range are shown in Fig. 5. Several broad

MnO_6 octahedra, and is usually found around 350 cm^{-1}. The highest energy mode (the stretching mode) originates from Mn−O bond stretching and it is usually positioned in 550−600 cm^{-1} range. In the case of manganites of rhombohedral structure ($R\bar{3}c$), which is of the lower symmetry, 8 IR active modes ($3A_u + 5E_u$) can be expected, among which three A_u and three out of five E_u modes originate from splitting of the degenerated F_{1u} modes [43]. For the orthorhombic structure (*Pnma*) of even lower symmetry, up to 25 IR active modes ($9B_{1u} + 7B_{2u} + 9B_{3u}$) can be expected. There are
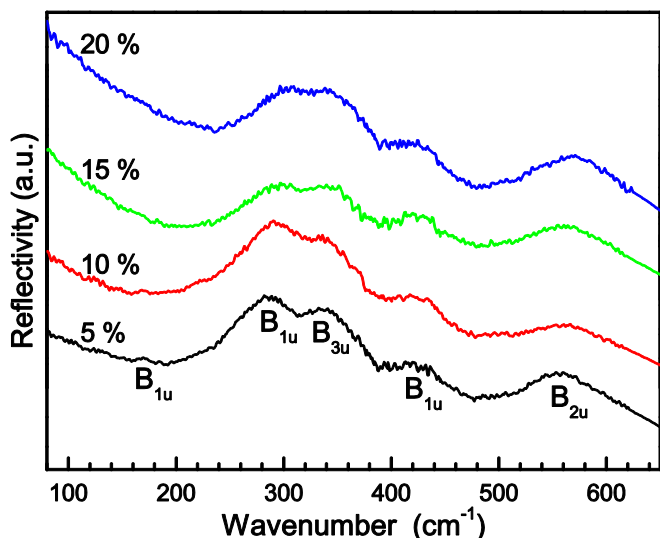
Fig. 5. Infrared reflectivity spectra of the $Ca_{1-x}Gd_xMnO_3$ ($x = 0.05, 0.1, 0.15, 0.2$) samples. The spectra are offset for clarity.

actually two variations of the orthorhombic structure, denoted as *Pnma-1* and *Pnma-2*. Both of them have the same symmetry, but *Pnma-1* is much less deformed.

Our samples have the *Pnma-1* structure. In this case, due to small deviation from the cubic structure, majority of the IR modes have small strength and cannot be well resolved. In addition to the previous work [44] on isostructural $LaMnO_3$, we have assigned two modes at 286/336 cm^{-1} as B_{1u}/B_{3u}, one mode at 416 cm^{-1} as B_{1u}, and one mode at 556 cm^{-1} as B_{2u}. With Gd doping, modes at 286 and 556 cm^{-1} are shifted to higher energies due to the change in the A-site ion radius with doping, and more importantly due to replacement of Mn^{4+} by Mn^{3+} as a consequence of Ca^{2+} substitution with Gd^{3+}. For higher doping contents, relative intensity of the mode at 336 cm^{-1} with respect to 286 cm^{-1} mode increases. The observed increase of 336 cm^{-1} mode intensity can be a consequence of higher sensitivity of this bending mode to the decrease in the Mn–O–Mn angle [45,46]. The increase of 336 cm^{-1} mode intensity, together with the shift of 286 cm^{-1} to higher energies, for higher doping levels appears as a partial merging of these two modes. The external mode, in manganites often found in 150–180 cm^{-1} range, is strongly screened in our samples by the Drude contribution, and is barely seen only in the 5% doped sample at about 168 cm^{-1} (B_{1u}). Sopracase et al. [46] have theoretically found that in the case of orthorhombic $CaMnO_3$, the low-energy external modes have a small dipole moment, resulting in small strength of the experimentally observed modes, which, together with strong Drude screening, can explain the absence of this mode in most of our samples.

3.4. Electron paramagnetic resonance (EPR) spectroscopy

Replacement of Ca^{2+} with Gd^{3+} causes reduction of Mn^{4+} to Mn^{3+}. Mn^{3+} ($3d^4$ with S = 2) is unlikely to have an observable EPR signal as it exhibits a large zero-field splitting because of the influence of the Jahn–Teller effect on the ^5E_g ground state in the octahedral symmetry.

The observed EPR signal is due to Mn^{4+}, but it cannot be attributed to isolated Mn^{4+} ions. EPR intensity and linewidth can be explained by a model in which a bottlenecked spin relaxation takes place from the constituent Mn^{4+} via the exchange-coupled Mn^{3+} Jahn–Teller ions to the lattice [47].

The measured room-temperature EPR spectra are shown in Fig. 6a. The six sharp lines in the EPR spectra are from the reference sample ZnS:Mn. The spectra shapes are of Lorentzian profile and do not saturate with EPR microwave power ($I(P^{1/2})$ is linear), which is indicated by homogenously broadened line, Fig. 6b.

The EPR linewidth seems to be a physical parameter that closely follows the cell distortion [48]. A weak increase of the line width (Table 7), with increasing Gd content is found, Fig. 7. The observed increase is much lower than the increase of linewidth found in $Ca_{1-x}Y_xMnO_3$ with increasing Y concentration [48]. It is associated with octahedral tilting that weakly depends on the concentration of Gd content (Table 1), compared with larger octahedra tilting increase observed in $Ca_{1-x}Y_xMnO_3$ [48]. The linewidth is inversely proportional to the relaxation time, which depends on interaction between Mn^{4+}–O–Mn^{3+}, which, on the other side, is angle dependent. The Mn–O–Mn angles are given in Table 1. Variation of the angles for our samples is relatively small.

While the line widths show a wide variety of behaviors depending on the temperature and concentration of divalent ions [49], and even on oxygen content [50], the g-factors are nearly constant and close to the free electron value. The g-factor of $Ca_{1-x}Gd_xMnO_3$, presented in Fig. 7. is close to the free electron value. The experimental error is estimated to be about 0.01 (due to high linewidth), which is comparable with the measured variation of g-factor.

Intensities of the lines in Fig. 6 were normalized for easier EPR spectra comparison. The actual intensities reading error was of the order of the expected trend of intensity change for various concentrations due to experimental issues [51], which prevented us from making a conclusion related to intensity.

The magnetization measurements performed on these samples showed that they are paramagnetic at room temperature and obeyed Curie-Weiss law at temperature above ~110 K. The magnetic moments obtained from Curie-Weiss law are in accordance with the theoretical values expected for the Mn^{4+}, Mn^{3+} and Gd^{3+}, and ratio of Mn^{4+}/Mn^{3+} is close to Ca^{2+}/Gd^{3+} ratio. So, there are no clusters of ions at room temperature, the EPR measurement temperature [52]. Clustering and ordering were observed at lower temperatures, T<~110 K. Samples with x = 0.05 or 0.10 show ferromagnetic transition and samples with x = 0.15 or 0.20 show antiferromagnetic transition [52].

The EPR signal, measured at liquid nitrogen temperature is not observed, because intensity of EPR diminishes and linewidth rises rapidly below ordering temperature $T_{C,N}$ [47,53].

4. Conclusion

We have used theoretical and experimental methods to investigate the octahedral tilting and related effects of $Ca_{1-x}Gd_xMnO_3$ ($x = 0.05, 0.1, 0.15, 0.2$) compound. Both methods have shown that orthorhombic-perovskite structure (space group *Pnma*) is the most stable form and according to Glazer's classification belongs to $a^-b^+a^-$ tilt system. Our bond valence calculations (BVC) have shown ten additional perovskite-related modifications of the equilibrium $Ca_{1-x}Gd_xMnO_3$ structure, and their stability has been investigated as function of Gd doping. We have further studied the influence of gadolinium amount on Mn–O bond angles and distances, tilting of MnO_6 octahedra around all three axes and deformation due to the presence of Jahn–Teller distortion around Mn^{3+} cation, and calculated the amount of Mn^{3+} in the system. Furthermore, our BVC approach is a simple, fast and efficient way of calculating the amount of Mn^{4+} and Mn^{3+} in the doped perovskite compound, which, to the best of our knowledge, has not been done before. The infrared reflection spectra of $Ca_{1-x}Gd_xMnO_3$ samples confirmed XRD results that $Ca_{1-x}Gd_xMnO_3$ nanopowders are of *Pnma-1*
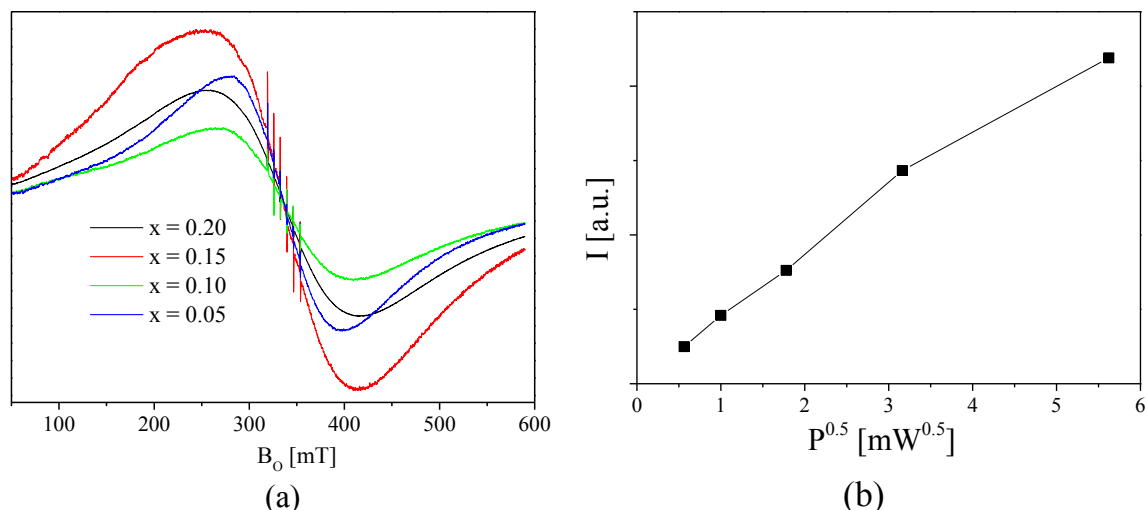
Fig. 6. (a) EPR spectra of $Ca_{1-x}Gd_xMnO_3$ ($x = 0.05, 0.1, 0.15, 0.2$) samples; (b) EPR Intensity vs. square root of the microwave power, for the $Ca_{0.8}Gd_{0.2}MnO_3$ sample.

Table 7
Parameters obtained from the EPR spectra, g-factor, intensity and linewidth (peak-to-peak).

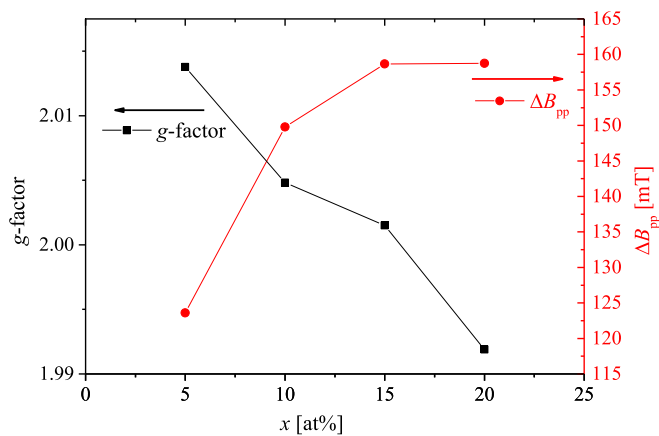| Sample	$Ca_{0.95}Gd_{0.05}MnO_3$	$Ca_{0.9}Gd_{0.1}MnO_3$	$Ca_{0.85}Gd_{0.15}MnO_3$	$Ca_{0.8}Gd_{0.2}MnO_3$
g-factor	2.014	2.005	2.0015	1.992
Int/Mass	6.4	5.7	15.2	9.5
ΔBpp	123.6	149.8	158.6	158.7

Fig. 7. Line widths and g-factors of observed EPR lines for various concentrations of $Ca_{1-x}Gd_xMnO_3$ samples.

structure and that the tilting of octahedra are increased with Gd doping. Finally, the EPR spectra are in accordance with the assumption that EPR linewidth is Mn–O–Mn angle dependent. The studied samples showed that small octahedra tilting in these samples brought only a small change of the EPR linewidth.

Acknowledgment

Appendix A. Supplementary data

Supplementary data related to this article can be found at http://dx.doi.org/10.1016/j.jallcom.2016.03.173.

References

[1] C.L. Bull, P.F. McMillan, Raman scattering study and electrical properties characterization of elpasolite perovskites $Ln_2(BB')O_6$ (Ln = La; Sm…Gd and B; B'=Ni, Co, Mn), J. Solid State Chem. 177 (2004) 2323–2328.
[2] Y.Q. Ma, W.H. Song, J. Yang, R.L. Zhang, B.C. Zhao, Z.G. Sheng, W.J. Lu, J.J. Du, Y.P. Sun, The current-induced effect on the Jahn–Teller distortion in the $La_{0.5}Ca_{0.5}MnO_3$ manganite, Solid State Commun. 133 (2005) 163–167.
[3] Y. Tomioka, Y. Okimoto, J.H. Jung, R. Kumai, Y. Tokura, Phase diagrams of perovskite-type manganese oxides, J. Phys. Chem. Solids 67 (2006) 2214–2221.
[4] P.M. Woodward, Octahedral tilting in perovskites. I. Geometrical consider-ations, Acta Cryst. B 53 (1997) 32–43.
[5] V.M. Goldschmidt, Die Gesetze der Krystallochemie, Naturwissenschaften 14 (1926) 477–485.
[6] D.A. Mota, Y.R. Barcelay, P.B. Tavares, M.R. Chaves, A. Almeida, J. Oliveira, W.S. Ferreira, J.A. Moreira, Competing exchanges and spin–phonon coupling in $Eu_{1-x}R_xMnO_3$ (R=Y, Lu), J. Phys. Condens. Mat. 25 (2013) 235602.
[7] E. Bose, S. Karmakar, B.K. Chaudhuri, S. Pal, C. Martin, S. Hébert, A. Maignan, Correlation of structural, magnetic and transport properties with the toler-ance factor in a low-doped $La_{0.875}Sr_{0.125-x}Ca_xMnO_3$, ($0 \leq x \leq 0.125$) system: cross-over from Mott to Shklovskii–Efros variable range hopping conduction, J. Phys. Condens. Mat. 19 (2007) 266218.
[8] J.B. Goodenough, Electronic and ionic transport properties and other physical aspects of perovskites, Rep. Prog. Phys. 67 (2004) 1915–1993.
[9] J.M.D. Coey, M. Viret, S. Von Molnar, Mixed-valence manganites, Adv. Phys. 48 (1999) 167–293.
[10] R.D. Shannon, Revised effective ionic radii and systematic studies of inter-atomic distances in halides and chalcogenides, Acta Cryst. A32 (1976) 751–767.
[11] E. Dagotto, T. Hotta, A. Moreo, Colossal magnetoresistant materials: the key role of phase separation, Phys. Rep. 344 (2001) 1–153.
[12] R., S.K. Mahendiran, A.K. Tiwary, T.V. Raychaudhuri, R. Ramakrishnan, N. Mahesh, C.N.R. Rangavittal, Rao, Structure, electron-transport properties, and giant magnetoresistance of hole-doped $LaMnO_3$ systems, Phys. Rev. B 53 (1996) 3348–3358.
[13] H.Y. Hwang, S.-W. Cheong, P.G. Radaelli, M. Marezio, B. Batlogg, Lattice effects on the magnetoresistance in doped $LaMnO_3$, Phys. Rev. Lett. 75 (1995)

914–917.

[14] J.L. García-Muñoz, J. Fontcuberta, B. Martínez, A. Seffar, S. Piñol, X. Obradors, Magnetic frustration in mixed valence manganites, Phys. Rev. B 55 (1997) R668–R671.

[15] J.L. García-Muñoz, J. Fontcuberta, M. Suaaidi, X. Obradors, Bandwidth narrowing in bulk $L_{2/3}A_{1/3}MnO_3$ magnetoresistive oxides, J. Phys. Condens. Mat. 8 (1996) L787–L793.

[16] N. Sharma, A.K. Nigam, R. Pinto, N. Venkataramani, S. Prasad, G. Chandra, S.P. Pai, Giant magnetoresistance studies on $La_{(0.8-x)}R_xSr_{0.2}MnO_3$ thin films (R = Pr, Nd, Gd, Ho), J. Magn. Magn. Mater 166 (1997) 65–70.

[17] J.M.D. Coey, M. Viret, S. von Molnar, Mixed-valence manganites, Adv. Phys. 48 (1999) 167–293.

[18] J.C. Schön, M. Jansen, First step towards planning of syntheses in solid-state chemistry: determination of promising structure candidates by global optimization, Angew. Chem. Int. Ed. Eng. 35 (1996) 1286–1304.

[19] D. Zagorac, J.C. Schön, J. Zagorac, M. Jansen, Prediction of structure candidates for zinc oxide as a function of pressure and investigation of their electronic properties, Phys. Rev. B 89 (2014) 075201.

[20] J. Zagorac, D. Zagorac, A. Zarubica, J.C. Schön, K. Djuris, B. Matovic, Prediction of possible $CaMnO_3$ modifications using an ab initio minimization datamining approach, Acta Cryst. B 70 (2014) 809–819.

[21] D. Zagorac, K. Doll, J.C. Schön, M. Jansen, Sterically active electron pairs in lead sulfide? An investigation of the electronic and vibrational properties of PbS in the transition region between the rock salt and the α-GeTe type modifications, Chem. Eur. J. 18 (2012) 10929–10936.

[22] D. Zagorac, J.C. Schön, M. Jansen, Energy landscape investigations using the prescribed path method in the ZnO system, J. Phys. Chem. C 116 (2012) 16726–16739.

[23] M.W. Lufaso, P.M. Woodward, Prediction of the crystal structures of perovskites using the software program SpuDS, Acta Cryst. B 57 (2001) 725–738.

[24] M.W. Lufaso, P.M. Woodward, Jahn-Teller distortions, cation ordering and octahedral tilting in perovskites, Acta Cryst. B 60 (2004) 10–20.

[25] R. Hundt, KPLOT-program, University of Bonn, Germany, 2012, 1979, Version 9, 6.15, www.crystalimpact.com/download/kplot.htm.

[26] R. Hundt, J.C. Schön, A. Hannemann, M. Jansen, Determination of symmetries and idealized cell parameters for simulated structures, J. Appl. Crystallogr. 32 (1999) 413–416.

[27] A. Hannemann, R. Hundt, J.C. Schön, M. Jansen, A new algorithm for space-group determination, J. Appl. Crystallogr. 31 (1998) 922–928.

[28] R. Hundt, J.C. Schön, M. Jansen, CMPZ – an algorithm for the efficient comparison of periodic structures, J. Appl. Crystallogr. 39 (2006) 6–16.

[29] R. Hundt, J.C. Schön, S. Neelamraju, J. Zagorac, M. Jansen, CCL: an algorithm for the efficient comparison of clusters, J. Appl. Crystallogr. 46 (Pt 3) (2013) 587–593.

[30] K. Momma, F. Izumi, VESTA: a three-dimensional visualization system for electronic and structural analysis, J. Appl. Crystallogr. 41 (2008) 653–658.

[31] M. Rosić, M. Logar, A. Devečerski, M. Prekajski, A. Radosavljević-Mihajlović, V. Kusigerski, V. Spasojević, B. Matović, Synthesis, structural and magnetic properties of nanostructured $Ca_{0.9}Gd_{0.1}MnO_3$ obtained by modified glycine nitrate procedure (MGNP), Ceram. Int. 37 (4) (2011) 1313–1319.

[32] M. Rosić, M. Logar, J. Zagorac, A. Devečerski, A. Egelja, V. Kusigerski, V. Spasojević, B. Matović, Investigation of the structure and the magnetic behaviour of nanostructured $Ca_{1-x}Gd_xMnO_3$ (x=0.05; 01; 0.15; 0.2) obtained by modified glycine nitrate procedure, Ceram. Int. 39 (2) (2013) 1853–1861.

[33] N.W. Thomas, A new global parameterization of perovskite structures, Acta Cryst. B 54 (1998) 585–599.

[34] G.A. Maris, Structural Transition Induced by Charge and Orbital Ordering in Transition Metal Oxides (Ph. D. thesis), University of Groningen, Netherlands, 2004.

[35] D.M. Sherman, The electronic structures of manganese oxide minerals, Am. Mineral. 69 (1984) 788–799.

[36] C. Silveira, M.E. Lopes, M.R. Nunes, M.E. Melo Jorge, Synthesis and electrical properties of nanocrystalline $Ca_{1-x}Eu_xMnO_{3\pm\delta}$ ($0.1\leq x\leq 0.4$) powders prepared at low temperature using citrate gel method, Solid State Ionics 180 (2010) 1702–1709.

[37] I. Matos, S. Serio, M.E. Lopes, M.R. Nunes, M.E. Melo Jorge, Effect of the sintering temperature on the properties of nanocrystalline $Ca_{1-x}Sm_xMnO_3$ ($0\leq x\leq 0.4$) powders, J. Alloys Compd. 509 (2011) 9617–9626.

[38] C.O. Paiva-Santos, R.F.C. Marques, M. Jafelicci Jr., L.C. Varanda, X-ray powder data and bond valence of $La_{0.65}Sr_{0.35}MnO_3$ after Rietveld refinement, Powder Diffr. 17 (2) (2002) 149–152.

[39] F. Mayr, C. Hartinger, M. Paraskevopoulos, A. Pimenov, J. Hemberger, A. Loidl, A.A. Mukhin, A.M. Balbashov, High-frequency conductivity and phonon properties of $La_{7/8}Sr_{1/8}MnO_3$, Phys. Rev. B 62 (2000) 15673–15679.

[40] A.V. Boris, N.N. Kovaleva, A.V. Bazhenov, A.V. Samoilov, N.-C. Yeh, R.P. Vasquez, Infrared optical properties of $La_{0.7}Ca_{0.3}MnO_3$ epitaxial films, J. Appl. Phys. 81 (1997) 5756–5758.

[41] A. Arulraj, C.N.R. Rao, An infrared spectroscopic study of the insulator-metal transition and charge-ordering in rare earth manganates, $Ln_{1-x}A_xMnO_3$ (Ln = rare earth, A = Ca, Sr, Pb), J. Solid State Chem. 145 (1999) 557–563.

[42] A.V. Boris, N.N. Kovaleva, A.W. Bazhenov, P.J.M. Van Bentum, Th Rasing, S.-W. Cheong, A.V. Samoilov, N.-C. Yeh, Infrared studies of a $La_{0.67}Ca_{0.33}MnO_3$ single crystal: optical magnetoconductivity in a half-metallic ferromagnet, Phys. Rev. B 59 (1999) R697–R700.

[43] G. De Marzi, Z.V. Popović, A. Cantarero, Z. Dohčević-Mitrović, N. Paunović, J. Bok, F. Sapiña, Effect of A-site and B-site substitution on the infrared reflectivity spectra of $La_{1-y}A_yMn_{1-x}B_xO_3$ (A=Ba,Sr; B=Cu,Zn,Sc; 0<y<=0.3; 0<=x<=0.1) manganites, Phys. Rev. B 68 (2003) 064302–064307.

[44] I.S. Smirnova, A.V. Bazhenov, T.N. Fursova, A.F. Dubovitskii, L.S. Uspenskaya, M.Y. Maksimuk, IR-active optical phonons in Pnma-1, Pnma-2 and R-3c phases of $LaMnO_{3+\delta}$, Phys. B 403 (2008) 3896–3902.

[45] I.S. Smirnova, Normal modes of the $LaMnO_3$ Pnma phase: comparison with $La2CuO4$ Cmca phase, Phys. B 262 (1999) 247–261.

[46] R. Sopracase, G. Gruener, E. Olive, J.-C. Soret, Infrared study of the phonon modes in $PrMnO_3$ and $CaMnO_3$, Phys. B 405 (2010) 45–52.

[47] A. Shengelaya, G.M. Zhao, H. Keller, K.A. Müller, EPR evidence of Jahn-Teller polaron formation in $La_{1-x}Ca_xMnO_{3+y}$, Phys. Rev. Lett. 77 (26) (1996) 5296–5299.

[48] D.L. Huber, G. Alejandro, A. Caneiro, M.T. Causa, F. Prado, M. Tovar, S.B. Oseroff, EPR linewidths in La1-xCaxMnO3: 0<~x<~1, Phys. Rev. B 60 (17) (1999) 12155–12161.

[49] J, Zagorac, S. Bošković, B. Matović, B. Babić-Stojić, structure and magnetic investigations of $Ca_{1-x}Y_xMnO_3$ (x=0, 0.1, 0.2, 0.3) and Mn4+/Mn3+ relation aanalysis, Sci. Sinter. 42 (2010) 221–232.

[50] C. Oliva, L. Forni, EPR and XRD as probes for activity and durability of $LaMnO_3$ perovskite-like catalysts, Catal. Commun. 1 (2000) 5–8.

[51] G.R. Eaton, S.S. Eaton, D.P. Barr, R.T. Weber, Quantitative EPR, A Practitioners Guide, Springer-Verlag Wien, 2010.

[52] M. Rosić, Lj Kljaljević, D. Jordanov, M. Stoiljković, V. Kusigerski, V. Spasojević, B. Matović, Effects of sintering on the structural, microstructural and magnetic properties of nanoparticle manganite $Ca_{1-x}Gd_xMnO_3$ (x = 0.05, 0.1, 0.15, 0.2), Ceram. Int. 41 (2015) 14964–14972.

[53] M.T. Causa, M. Tovar, R.D. Zysler, M. Vallet-Regi, J.M. Gonzales-Calbet, R.D. Sanchez, J. Phys. IV 07 (1997) C1–C355.